

Ceci n'est pas un committor, yet it samples like one: efficient sampling via approximated committor functions.

Enrico Trizio,^{1, a)} Giorgia Rossi,¹ and Michele Parrinello^{*1, b)}

¹*Atomistic Simulations, Italian Institute of Technology, 16156 Genova, Italy*

(Dated: 27 February 2026)

Atomistic simulations are widely used to investigate reactive processes but are often limited by the rare event problem due to kinetic bottlenecks. We recently introduced an enhanced sampling approach based on the committor function, machine-learned following a variational principle. This method combines a transition-state-oriented bias potential, expressed as a functional of the committor, with a metadynamics-like bias along a committor-based collective variable, enabling uniform exploration of reaction pathways. In its original formulation, the committor is represented by a neural network that takes physical descriptors as input and is trained by minimizing a functional involving gradients with respect to atomic coordinates, which can be computationally demanding in some cases. Here, we propose a simplified learning criterion formulated entirely in the descriptor space, which bypasses the need for explicit and costly coordinate gradients and provides a relaxed upper bound to the original variational principle. Although this approach does not formally target the *exact* committor, we show that it retains robust sampling performance while significantly reducing computational costs, thus enabling the study of processes that would be practically unfeasible using the original formulation.

I. INTRODUCTION

Atomistic simulations are one of the pillars of modern science, enabling the study of the microscopic mechanisms underlying reactive processes in fields as diverse as biophysics, materials science, and chemistry. However, the scope of such methods is still limited by the timescales accessible to standard simulation algorithms, which are typically much shorter than those of most reactive processes, making them difficult to observe in simulations.¹ This is due to the so-called rare event problem, which arises when metastable states are separated by kinetic bottlenecks. To address this issue, over the last few decades, several enhanced sampling methods aimed at facilitating the study of rare events have been developed.^{2,3}

Recently, we introduced a promising method^{4,5} based on the calculation of the committor function combined with the On-the-fly Probability Enhanced Sampling (OPES) method.^{6,7} This approach has demonstrated unique capabilities in uniformly sampling entire reaction pathways and has several merits: it is based on a physics-grounded variational principle, it enables exhaustive sampling of the transition state (TS) region, and it provides a powerful tool to reveal the reaction process in remarkable detail. In the method section, we summarize the key concepts of this approach, while a more extensive discussion can be found in the original papers.^{4,5}

The central quantity of this approach is the committor function $q(\mathbf{x})$, which, for the transition between two states A and B, gives the probability that a configuration \mathbf{x} evolves to state B before having first passed by A.⁸ Owing to this probabilistic description, the committor is

widely considered to provide the ideal description of a reactive process, and due to its many attractive features, much work has been done to determine it.^{9–21} However, computing $q(\mathbf{x})$ is challenging, as it requires extensive sampling of the TS region. Traditionally, this was obtained either from long simulations²² or via transition path sampling.^{20,23–25} Recently, we have shown that once the A and B states are known, the committor can be computed via a self-consistent iterative procedure.^{4,5} Our approach is based on a variational principle first pioneered by Onsager²⁶ and later framed into the formalism of Kolmogorov's backward equation.²⁷ This principle states that, under the assumption of overdamped Langevin dynamics, the committor can be determined by imposing the boundary conditions $q(\mathbf{x}_{i \in A}) = 0$ and $q(\mathbf{x}_{i \in B}) = 1$ and minimizing the functional

$$K[q(\mathbf{x})] = \langle |\nabla_{\mathbf{u}} q(\mathbf{x})|^2 \rangle$$

in which the gradients $\nabla_{\mathbf{u}}$ are computed with respect to the mass-scaled atomic coordinates and $\langle \cdot \rangle$ denotes the average over the equilibrium Boltzmann ensemble.

In Ref. 5, the committor was expressed as a feed-forward neural network $q_{\theta}(\mathbf{d}(\mathbf{x}))$, where θ are learnable parameters. The input of the neural network is a set of N_d physical descriptors $\mathbf{d}(\mathbf{x})$ which provide a convenient way to enforce the system's physical symmetries and favor interpretability. The model parameters are optimized using as a loss function the $K[q(\mathbf{x})]$ functional supplemented by the above-mentioned boundary conditions.

Due to its ability to extensively and uniformly sample the reactive process, our approach has proven robust and successful in applications that range from biophysics^{5,28,29} to chemistry and materials science.^{4,5,30} However, in some cases, training the committor can be rather expensive. The main numerical source of inefficiency is often the calculation of the gradients relative to the atomic coordinates in the variational functional. The cost of computing

^{a)}enrico.trizio@iit.it

^{b)}michele.parrinello@iit.it

these derivatives can be rather high when using complex descriptors that depend on a large number of atoms.^{30,31}

The aim of this paper is to reduce the computational cost of this part of the calculation while retaining its overall sampling efficiency. To this effect, we replace the original functional with a new one that depends only on the derivatives of the committor relative to the descriptors

$$\tilde{K}[q(\mathbf{d}(\mathbf{x}))] = \langle |\nabla_{\mathbf{d}} q(\mathbf{d}(\mathbf{x}))|^4 \rangle_{\mathbf{U}(\mathbf{x})}$$

This choice can be motivated with the help of the Cauchy-Schwarz inequality, showing that $\tilde{K}[q(\mathbf{d}(\mathbf{x}))]$ is an upper bound to $K[q(\mathbf{d}(\mathbf{x}))]^2$.

Even if this approach does not lead to computing the *true* committor, we show that it provides a reliable and economical sampling tool across a number of paradigmatic examples, including the conformational equilibrium of alanine dipeptide, an intramolecular proton transfer reaction, a binding problem, and the crystallization of silicon from melt, some of which would have been unfeasible with the original approach. We hope that this clarifies the title of the manuscript, which is inspired by the painting *Ceci n'est pas une pipe* (This is not a pipe) by the surrealist painter René Magritte, which, ironically, represents a pipe.

II. METHODS

In the following, we start by giving an overview of the whole iterative procedure in Sec. II A, highlighting the key differences with Ref. 5. Then, we discuss in detail all the components of such a procedure. Specifically, in Sec. II B, we recall the general features of the committor function and the main concepts of the original approach of Ref. 5. Then, in Sec. II C, we present in detail the modifications to the variational loss function used for the optimization of the approximated committor models.

A. Summary of the self-consistent iterative procedure.

Here, we outline the steps of the self-consistent iterative procedure proposed here for the learning of approximated committor functions. Such a procedure closely resembles the original recipe of Ref. 5, except for the use of a different loss function that leads to an approximated committor model, as detailed in the following sections.

- **Step 1:** At iteration n , the committor model $q_0^n(\mathbf{x})$ is trained on the dataset of configurations \mathbf{x}^n and weights \mathbf{w}^n accumulated up to iteration n . In the first iteration, i.e., $n = 0$, the dataset is either composed of data from previous calculations or solely of labeled configurations from the metastable basins. The optimization of the model is performed by minimizing the modified loss functions in Eqs. 13 and 12.

- **Step 2:** The committor estimate is used to perform enhanced sampling simulations under the combined action of the Kolmogorov bias V_K^n and the OPES bias V_{OPES}^n . The latter is applied along the committor-related CV $z^n(\mathbf{x})$.

- **Step 3:** The sampled configurations are used to update the training dataset after being reweighted according to the effective bias $V_{\text{eff}}^n = V_K^n + V_{\text{OPES}}^n$ with weights given by $w_i^n = \frac{e^{\beta V_{\text{eff}}^n(\mathbf{x}_i)}}{\langle e^{\beta V_{\text{eff}}^n(\mathbf{x})} \rangle_{\mathbf{U}_{\text{eff}}^n}}$.

The above steps are iterated to refine the committor estimate and improve sampling until convergence is reached.

B. Background

Committor function. As mentioned in the introduction, given two metastable states A and B, the committor $q(\mathbf{x})$ is a function of the atomic coordinates \mathbf{x} which returns the probability that a trajectory initiated from configuration \mathbf{x} will reach state B before passing through A. As a consequence, the committor resembles a step-like function, being nearly constant in the metastable basins, i.e., $q(\mathbf{x}_{i \in A}) \simeq 0$ and $q(\mathbf{x}_{i \in B}) \simeq 1$, and displaying significant gradients only over the TS region. Due to its probabilistic nature, the committor is arguably the most principled description of a reactive process, and it is believed to be an ideal reaction coordinate.⁸

However, determining the committor is challenging. One possibility is to leverage a variational approach pioneered by Onsager and later formalized using the Kolmogorov backward equation, which states that, given the boundary conditions $q(\mathbf{x}) = 0$ for $\mathbf{x} \in A$ and $q(\mathbf{x}) = 1$ for $\mathbf{x} \in B$, the committor can be obtained by minimizing the functional

$$K[q(\mathbf{x})] = \langle |\nabla_{\mathbf{u}} q(\mathbf{x})|^2 \rangle \quad (1)$$

where $\langle \cdot \rangle$ denotes the average on the Boltzmann ensemble associated with the interatomic potential $\mathbf{U}(\mathbf{x})$, and $\nabla_{\mathbf{u}}$ the gradient with respect to the mass-weighted coordinates \mathbf{u} . Unfortunately, even if Eq. 1 could be evaluated through sampling, its practical application remains challenging due to the strong localization of $|\nabla q(\mathbf{x})|$ on the TS region, which is highly unfavored in simulations.

Kolmogorov bias. To overcome the sampling limitations associated with the TS in rare events, in Ref. 4, we introduced the Kolmogorov bias potential $V_K(\mathbf{x})$ to stabilize the TS region and favor its sampling. This TS-oriented bias is defined as a functional of the committor, exploiting the strong localization of its gradients on the TS

$$V_K(\mathbf{x}) = -\frac{\lambda}{\beta} \log(|\nabla q(\mathbf{x})|^2 + \epsilon) \quad (2)$$

where $\beta = \frac{1}{k_B T}$ is the inverse temperature and λ a parameter regulating the magnitude of the bias. In turn, ϵ is a

regularization term that can either simply avoid numerical instabilities (i.e., $\epsilon \ll 1$) or filter out contributions with negligible $|\nabla q(\mathbf{x})|$ (i.e., $\epsilon = 1$). In this work, as a safety measure, we opted for the latter option to avoid possible artifacts in the metastable regions.

In practice, when applying $V_K(\mathbf{x})$ in enhanced sampling calculations, one can equivalently compute it considering the gradients with respect to the atomic coordinates or to the input descriptors, as discussed in Ref. 4. As the second possibility is simpler to implement and computationally cheaper, it is to be preferred.

The bias $V_K(\mathbf{x})$ is attractive where $|\nabla q(\mathbf{x})|$ is large, thus, in the biased energy landscape $U_K(\mathbf{x}) = U(\mathbf{x}) + V_K(\mathbf{x})$, the TS region is stabilized and its sampling is favored. Furthermore, $U_K(\mathbf{x})$ can be used to define the Kolmogorov probability distribution as

$$p_K(\mathbf{x}) = \frac{e^{-\beta U_K(\mathbf{x})}}{Z_K} \quad \text{with} \quad Z_K = \int e^{-\beta U_K(\mathbf{x})} d\mathbf{x} \quad (3)$$

which offers a practical way to identify the transition state ensemble (TSE).^{4,5,28,29}

Machine learning the committor. In Ref. 5, we leveraged the variational principle of Eq. 1 to optimize a machine-learning-based parametrization of the committor through a self-consistent iterative procedure. During such a procedure, cycles of (enhanced) sampling and training are alternated to progressively improve both the committor estimate and the sampling until convergence is reached.

As far as the learning part is concerned, the committor is represented as a feedforward neural network (NN) $q_\theta(\mathbf{x}) = f_\theta(\mathbf{d}(\mathbf{x}))$ with trainable parameters θ , taking as input a set of physical descriptors $\mathbf{d}(\mathbf{x})$. These descriptors, in turn, are designed to capture the essential degrees of freedom of the system, enforce required symmetries, and incorporate prior physical information. In addition, in order to impose the correct functional form on the output, we apply a sigmoid-like activation function σ to the raw output $z(\mathbf{x})$ of the NN, thus obtaining the committor as

$$q(\mathbf{x}) = \sigma(z(\mathbf{x})) \quad (4)$$

The network parameters are optimized by minimizing a loss function composed of two contributions. One is the *boundary loss* term, which imposes the correct boundary conditions, and is computed on a labeled dataset of configurations from the initial and final states. The other is the *variational loss* term, which is based on the variational functional of Eq. 1 and is evaluated on the data obtained via enhanced sampling simulations.

The simulations run during the iterative procedure are driven by two complementary bias potentials. On the one hand, the TS-oriented Kolmogorov bias $V_K(\mathbf{x})$ (see Eq. 2) is employed to stabilize the TS region to favor its sampling. On the other hand, a metadynamics-like bias, based on the On-the-fly probability enhanced sampling^{6,7} (OPES) framework, is used to smooth out the free energy landscape, thereby favoring transitions between states and ergodic sampling. In practice, the OPES bias uses

$z(\mathbf{x})$ as a CV rather than $q(\mathbf{x})$, since it encodes the same information as $q(\mathbf{x})$, but has a smoother behavior that makes it more suitable for this application.

C. Reformulation of variational loss

While the procedure summarized above provides a reliable framework that has already been successfully applied to a range of systems,^{4,5,28–30,32} it still presents some practical drawbacks in certain cases. Indeed, during training, the main computational cost arises from the minimization of the variational term, which requires computing the gradients $\nabla_{\mathbf{u}} q_\theta(\mathbf{x})$ with respect to the mass-scaled atomic positions \mathbf{u} , which in many applications may become particularly demanding. Specifically, using automatic differentiation packages,³³ the computational load of the training is proportional to i) the number of descriptors used, ii) their complexity, and iii) the number of atoms involved in the calculation of such descriptors. Even if this is not a conceptual limitation and strategies to reduce the overload can be devised, in practice, this can introduce an extra layer of complexity. This motivated us to seek a reformulation of our learning approach that would reduce the computational burden and simplify the set up protocol.

To this aim, we start by splitting $\nabla_{\mathbf{u}} q_\theta(\mathbf{x})$ into two contributions using the chain rule of differentiation

$$\nabla_{\mathbf{u}} q_\theta(\mathbf{x}) = \nabla_{\mathbf{u}} \mathbf{d}(\mathbf{x}) \nabla_{\mathbf{d}} q_\theta(\mathbf{x}) \quad (5)$$

thus decoupling the derivatives with respect to mass-weighted positions $\nabla_{\mathbf{u}}$ and descriptors $\nabla_{\mathbf{d}}$. Notably, only the latter contribution depends on the NN model's variational parameters θ , and thus changes during training, whereas the former does not change as the model is updated, as it is fully determined by the choice of descriptors. In addition, computation of the $\nabla_{\mathbf{u}} \mathbf{d}(\mathbf{x})$ matrix can be both computationally expensive, as its size scales with the number of atoms involved in the descriptors calculation, and inefficient, as only a few atoms contribute to each descriptor, thus typically making it extremely sparse.

Both these considerations suggest that a learning criterion can be devised based only on $\nabla_{\mathbf{d}} q_\theta(\mathbf{x})$, trading a reasonable approximation for potentially large computational savings. Besides this somewhat naive intuition, such an alternative approach can also be formally backed by finding an upper bound to the original variational principle, as we now proceed to discuss. For simplicity of notation, from now on, we omit the θ subscript when referring to the parametrization of the committor, i.e., $q_\theta(\mathbf{x}) \rightarrow q(\mathbf{x})$.

Making the dependence on the input descriptors explicit, the Kolmogorov functional of Eq. 1 can be expressed as

$$K[q(\mathbf{d}(\mathbf{x}))] = \langle |\nabla_{\mathbf{u}} q(\mathbf{d}(\mathbf{x}))|^2 \rangle \quad (6)$$

which, after simple manipulations, fully detailed in the SI, can be written as

$$\mathbf{K}[q(\mathbf{d}(\mathbf{x}))] = \langle \mathbf{g}_{i,j} \mathbf{k}_{i,j} \rangle \quad (7)$$

where

$$\mathbf{g}_{i,j} = \frac{\partial d_i}{\partial \mathbf{u}_{l,n}} \frac{\partial d_j}{\partial \mathbf{u}_{l,n}} \quad \mathbf{k}_{i,j} = \frac{\partial q}{\partial d_i} \frac{\partial q}{\partial d_j} \quad (8)$$

In the above equation, the Einstein summation convention over repeated indices is implied, and the indices l and n refer, respectively, to the N atom coordinates and their Cartesian components, while i and j run over the N_d descriptors.

This reformulation allows the Cauchy-Schwarz inequality to be applied, leading to

$$\langle \mathbf{g}_{i,j} \mathbf{k}_{i,j} \rangle^2 \leq \langle \mathbf{g}_{i,j} \mathbf{g}_{j,i} \rangle \langle \mathbf{k}_{i,j} \mathbf{k}_{j,i} \rangle \quad (9)$$

In this expression, the purely geometric term $\langle \mathbf{g}_{i,j} \mathbf{g}_{j,i} \rangle$ is decoupled from the model-dependent term $\langle \mathbf{k}_{i,j} \mathbf{k}_{j,i} \rangle$ that only depends on the committor derivatives with respect to the descriptors. Thus, the latter can be used as a new and simplified objective function for model optimization. Remarkably, this formulation avoids explicitly evaluating the descriptor gradients with respect to the atomic coordinates, leading to a significantly reduced computational cost.

In addition, using elementary algebra, computing this term can be further simplified. Specifically, defining the vector

$$\mathbf{h} = \begin{pmatrix} \frac{\partial q}{\partial d_1} \\ \vdots \\ \frac{\partial q}{\partial d_{N_d}} \end{pmatrix} \quad (10)$$

and writing matrix \mathbf{K} as the outer product $\mathbf{K} = \mathbf{h} \mathbf{h}^T$, we can obtain a simpler expression for the new variational component of the loss function as

$$\langle \mathbf{k}_{i,j} \mathbf{k}_{j,i} \rangle = \langle \text{tr}(\mathbf{K}^2) \rangle = \langle \|\mathbf{h}\|^4 \rangle \quad (11)$$

which depends only on the derivatives of the committor with respect to the descriptors.

During training, Eq.11 is used as a variational loss L_v , which is evaluated on a dataset of N_v configurations from enhanced sampling simulations according to

$$L_v = \frac{1}{N_v} \sum_i w_i |\nabla_{\mathbf{d}} q(\mathbf{x}_i)|^4 \quad (12)$$

where $w_i = \frac{e^{\beta V_{\text{eff}}(\mathbf{x}_i)}}{\langle e^{\beta V_{\text{eff}}(\mathbf{x})} \rangle_{U_{\text{eff}}}}$ are statistical weights to reweigh each configuration \mathbf{x}_i by the total bias $V_{\text{eff}} = V_K + V_{\text{OPES}}$ to its corresponding Boltzmann probability.

This loss is complemented by the same boundary term L_b used in the original recipe, which is expressed as

$$L_b = \frac{1}{N_A} \sum_{i \in A} q(\mathbf{x}_i)^2 + \frac{1}{N_B} \sum_{i \in B} (q(\mathbf{x}_i) - 1)^2 \quad (13)$$

and is evaluated on a labeled dataset of N_A and N_B configurations collected by running short, unbiased MD simulations in the two basins. The overall optimization of the network parameters is then performed by minimizing a combination of the two losses $L = L_v + \alpha L_b$, where the α hyperparameter scales the relative magnitude of the two contributions.

As a final practical note, we recall that, for improved numerical stability, it is also possible to minimize $\log(L)$, as proposed in Ref. 30. In addition, we found that the new learning objective is more prone to overfitting in some cases. It is thus advisable to monitor this behavior and, if necessary, adopt strategies to avoid it, e.g., via early stopping or shorter training.

III. RESULTS

A. Alanine Dipeptide conformational equilibrium

The first test system for our methodology was the conformational equilibrium of alanine dipeptide, often used as a benchmark for new enhanced sampling methods (see Fig. 1A). As often done in the past for this molecule, we

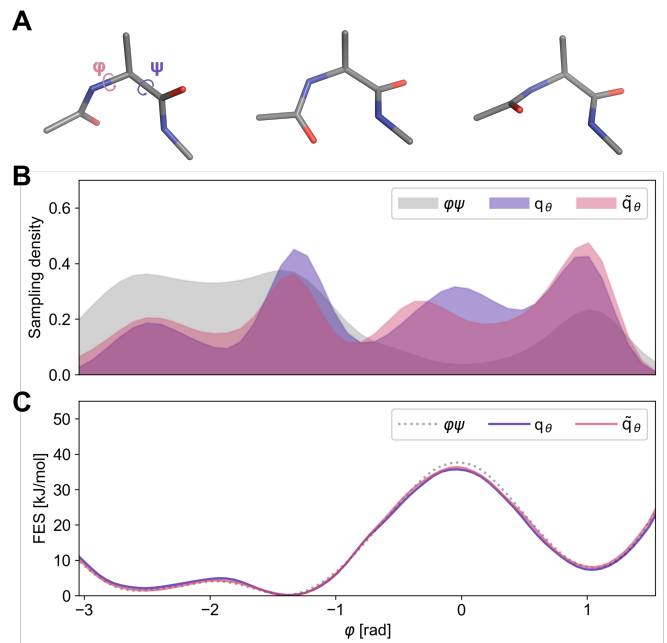


FIG. 1. **Alanine dipeptide isomerization.** **A.** Representative snapshots of the isomerization process. **B.** Sampling density distribution projected along the ϕ torsional angle. **C.** Free energy surface (FES) plotted along the ϕ torsional angle. In panels **B** and **C**, results obtained with a standard OPES run using ϕ and ψ torsional angles as CVs are reported in grey, those obtained with OPES+ V_K based on a committor model trained following the original variational approach (q_θ) are reported in purple, and those obtained with OPES+ V_K based on a committor model trained following the simplified variational approach (\tilde{q}_θ) are reported in pink.

use the interatomic distances between the heavy atoms of the molecule as input descriptors.^{5,34,35} Based on this description of the system, we set up our simplified approach, obtaining an approximated committor function, which was used to drive enhanced sampling calculations with the OPES and Kolmogorov biases. This provided effective sampling of the entire relevant phase space by promoting frequent transitions between the metastable states (see Fig. 1B). From the data thus collected, we recovered accurate free energy estimates that were almost indistinguishable from those obtained using as CVs the conventional φ - ψ torsional angles or a committor model trained on the original variational approach (see Fig. 1C).

Notably, our calculations also retained a strong focus on the TS region, whose sampling is greatly enhanced if compared with a standard OPES run (see Fig. 1B). Nonetheless, the sampling density is not exactly centered on the *true* transition state, which is located at $\varphi \sim 0$. Even if in terms of sampling, this is only a minor sacrifice, for completeness, one may be interested in obtaining a more accurate estimate of the committor for further analysis. To this end, it is possible to use the cheaply generated data from the simplified approach to perform a single additional iteration using the original, more expensive variational approach, without the need for multiple calculations. As expected, the results obtained with the original strategy are slightly better in terms of TS sampling, but remarkably, no differences can be seen in the FES estimate.

However, it must be noted that, even on a system as simple as alanine and with a limited set of simple descriptors, the training time using the original formulation was roughly 3 times higher than using the simplified one, thus motivating the use of the latter, especially for more complex systems.

B. Proton transfer in tropolone

As a second test case, we studied the intramolecular proton transfer (PT) involved in the isomerization of tropolone, a small aromatic molecule. The aromatic ring of this molecule is substituted with two adjacent oxygens, which, depending on the specific isomer, can be found either in the hydroxyl or keto form (see Fig. 2A). In addition, two other minor metastable states are present, determined by the relative orientation (inward or outward) of the H of the hydroxyl group with respect to the keto oxygen.

Here, the input descriptors used were the interatomic distances involving the heavy atoms and those between the reactive H and O atoms. The four metastable states mentioned above are clearly distinguishable in the FES estimate obtained with our method (see Fig. 2B). As expected, the FES is also symmetric, as the two oxygens are equivalent, and the free energy difference between the two isomers quickly converges to the correct value $\Delta G = 0$ kJ/mol (see Fig. 2C).

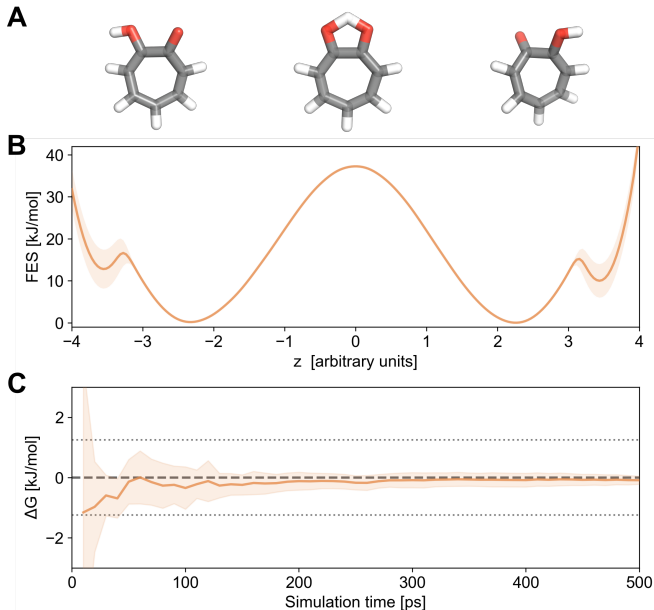


FIG. 2. **Proton transfer in tropolone.** **A.** Representative snapshots of the reaction stages, with the transition state characterized by the shared proton between the two oxygens. **B.** Free energy surface (FES) plotted along the learned z CV. **C.** Convergence with simulation time of the estimated free energy difference between the two main isomers. The dashed line shows the reference value, with the $\pm 0.5 k_B T$ interval marked by the thin dotted lines. In panels **B** and **C**, average values obtained from 3 independent simulations are depicted as solid lines, whereas the corresponding standard deviations are shown as shaded areas.

C. OAMe-G2 binding

If the first two examples could have been handled with the original approach at only a moderate additional computational cost, we now move to systems where that would have been more problematic. One such case is the ligand-binding process in solution, in which it is necessary to account for the solvent role in the dynamics of both the binding pocket and the ligand itself. Unfortunately, as the solvent molecules are indistinguishable and highly mobile, applying the original approach requires an explicit dependence of the model on a large number of atoms. At best, this limitation introduces several practical issues in handling and processing data related to many atoms, which can easily saturate available computing memory and dramatically slow down training. Indeed, even in simplified systems with a limited number of atoms and solvent molecules, as the one discussed here, the original approach can be orders of magnitude slower than the simplified one proposed here. In even more complex scenarios, the limitations of the original framework make its application unfeasible in practice.

As a prototypical example of this class of processes, we studied the binding of the G2 molecule to the OAMe calixarene guest from the SAMPL5 challenge,³⁶ which has

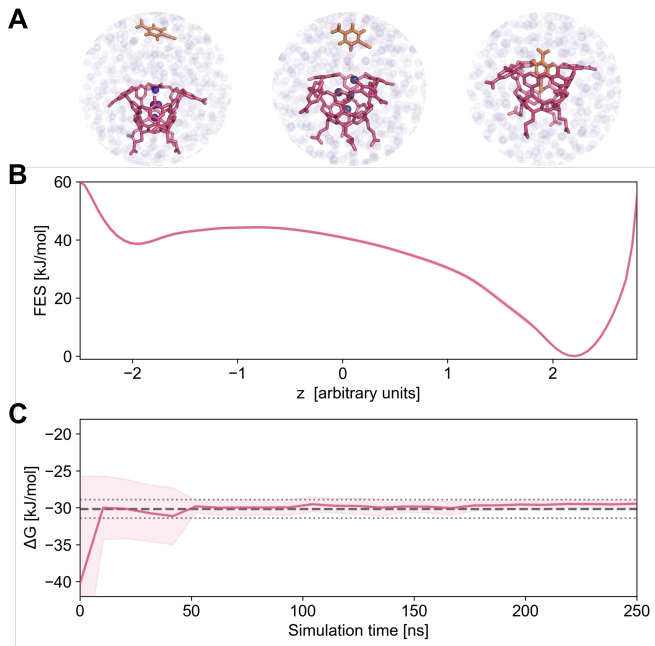


FIG. 3. **G2-OAME binding.** **A.** Representative snapshots of the binding stages, with the host molecule colored in pink and the guest in orange. Water molecules are represented as blue spheres in solid color when inside the pocket, and transparent otherwise. **B.** Free energy surface (FES) plotted along the learned z CV. **C.** Convergence with simulation time of the estimated binding energy. The dashed line shows the reference value obtained with the same setup as Ref. 38, with the $\pm 0.5 k_B T$ interval marked by the thin dotted lines. In panels **B** and **C**, average values obtained from 3 independent simulations are depicted as solid lines, whereas the corresponding standard deviations are shown as shaded areas.

been extensively characterized in several papers^{5,37–39} (see Fig. 3A). As done in Refs. 38 and 5, we chose to treat the solvation degrees of freedom separately from the trivial positional ones. To this end, we trained our model solely on water coordination numbers, computed for a few ligand atoms and a set of virtual atoms above the binding pocket, and biased the resulting committor-like CV using both OPES and $V_{\kappa}(\mathbf{x})$. Specifically, the OPES component of the bias was applied to both the committor-based CV $z(\mathbf{x})$ and the ligand-pocket distance. Following this strategy, we were able to promote efficient sampling and obtain accurate free energy estimates in good agreement with previous studies with a similar computational setup (see Fig. 3B and C).

It must be noted that, even with the relatively simple setup and the limited scale of this system, in order to use the old formulation, one would have needed to track, and thus print to file, the positions of a few hundred water molecules per frame. In contrast, with the approach proposed in this work, the required data is reduced to the simple set of 12 coordination numbers used as descriptors, whose storage is negligible even for long trajectories. Most remarkably, the new scheme led to a 100-fold reduction

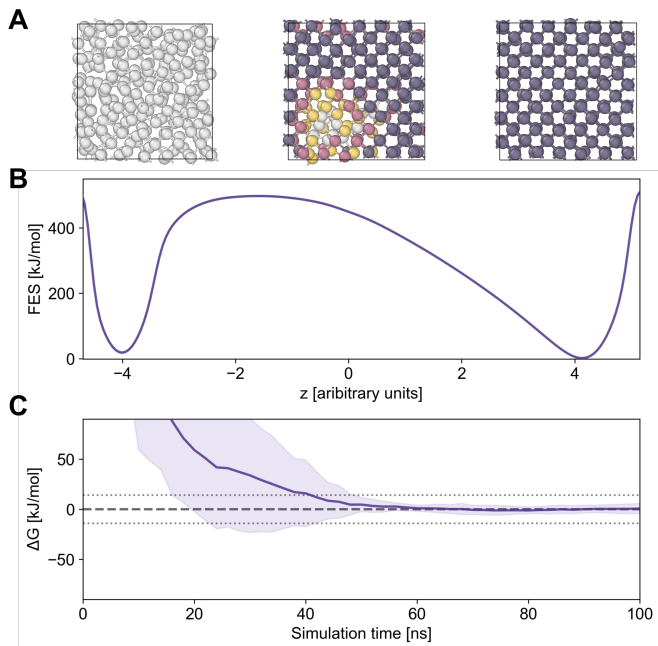


FIG. 4. **Silicon crystallization.** **A.** Representative top-view snapshots of the crystallization process from the disordered liquid phase to the ordered solid. Atoms are colored according to the degree of similarity of their local arrangement to the ideal diamond structure. The darker the color, the higher the similarity. **B.** Free energy surface (FES) plotted along the learned z CV. **C.** Convergence with simulation time of the estimated free energy difference between the two states. The dashed line shows the reference value, with the $\pm k_B T$ interval marked by the thin dotted lines. In panels **B** and **C**, average values obtained from 3 independent simulations are depicted as solid lines, whereas the corresponding standard deviations are shown as shaded areas.

in the training computational burden while still retaining a more than satisfactory sampling.

D. Crystallization of Si

As a final test case, we studied the crystallization of silicon to its diamond structure close to the melting temperature ($T=1700\text{K}$), a scenario where the practical advantages of our new approach are most evident (see Fig. 4A). In fact, when studying phase transitions, it is necessary to properly account for symmetries and local atomic arrangements, which typically requires descriptors that are complex, many-body functions of the atomic coordinates, such as the Steinhardt order parameters, and possibly depend on *all* the particles in the simulation box, for example, radial density functions or x-ray diffraction peak intensities.⁴⁰ This would clearly represent a significant bottleneck within the original framework, but becomes negligible with our new formulation.

Indeed, following Ref. 41, we employed as input descriptors the peaks of the anisotropic structure factor of silicon.

In this case, considering the different relative magnitudes of these inputs, we also introduced a preprocessing normalization layer to the NN architecture. In addition, to make up for the expected larger free energy barrier and the considerably high temperature, we used a larger λ value, i.e., $\lambda = 1000$.

Even starting from data limited to the pure phases, our iterative procedure allowed us to progressively learn an effective reaction coordinate, which correlates well with the commonly used, but rather expensive, CVs based on environment similarity⁴² and Steinhardt parameters (see SI, Fig. S7).

Remarkably, also for this more complex process, many reactive events were observed. From such data, it was possible to recover accurate free energy estimates (see Fig. 4B), with the two phases found at the same relative free energy, as expected when being at the melting temperature (see Fig. 4C).

IV. DISCUSSION

This paper fits into a broader effort to extend enhanced sampling methods to the detailed study of transition states and to make them more automated and accessible. In Refs. 4 and 5, we leveraged machine learning together with the longstanding formal theory of the committor function to achieve first extensive sampling of the TS region, and later uniform and ergodic sampling of the relevant phase space. With Ref. 32, we moved a step further toward automation by exploiting the expressive power of graph neural networks to operate directly on atomic coordinates, thereby bypassing the need for manually designed input descriptors, although at a higher computational cost.

In this work, we focus on accessibility and scalability, introducing a controlled approximation of the committor function to dramatically reduce the practical barrier to use. By reframing the learning procedure as a simpler variational problem, we reduce the optimization complexity and its associated computational cost, achieving orders-of-magnitude savings in training time. This reduction is particularly impactful in more complex systems, making the approach feasible when it would otherwise be prohibitive. At the same time, even for simpler cases, the approximated formulation yields a more streamlined workflow, significantly simplifying the setup and accelerating calculations, making it naturally suitable for automated, scalable computational pipelines.

These advantages, however, come with a trade-off that should be acknowledged, as the new formulation does not formally target the *true* committor function, a defining feature of the original approach and central to its use in detailed mechanistic analysis. Nonetheless, when no other viable option is available, the approximated committor can still provide valuable insight as well as clear sampling advantages. In particular, an estimate of the original variational functional, informative of kinetic rates, can be recovered from the approximated model with a sin-

gle calculation and without any additional optimization, leveraging Eq. 7.

From a broader perspective, the proposed framework can also serve as an entry point within multistage workflows. It can be deployed as a fast and robust sampling engine during early exploration of complex or computationally intensive systems, providing an initial characterization at a fraction of the cost. Subsequently, the formally exact but more demanding approach can be adopted for final production simulations and in-depth analysis.

Overall, this work represents an important step toward making committor-based enhanced sampling practical at scale. By significantly lowering the computational cost while mostly retaining the original framework’s sampling power, the proposed approach extends the reach of TS-focused simulations and contributes to consolidating committor-based methods as a scalable tool within the enhanced sampling toolbox for the study of complex systems.

CODE AND DATA AVAILABILITY

The committor models have been trained using the open-source library `mlcolvar`.⁴³ Enhanced sampling simulations have been performed using a custom interface for the PLUMED⁴⁴ plugin for enhanced sampling and free energy calculations. Simulation inputs and the code needed for training and performing enhanced sampling simulations will be made available on GitHub upon publication.

ACKNOWLEDGMENTS

The authors are grateful to Luigi Bonati, Florian Dietrich, Ioannis Galdadas, and Alice Triveri for useful feedback and discussions on the manuscript.

COMPETING INTERESTS STATEMENT

The authors declare no competing interests.

REFERENCES

- ¹D. Frenkel and B. Smit, *Understanding molecular simulation: from algorithms to applications*, Vol. 1 (Elsevier, 2001).
- ²J. Hémin, T. Lelièvre, M. R. Shirts, O. Valsson, and L. Delmotte, “Enhanced sampling methods for molecular dynamics simulations,” *Living Journal of Computational Molecular Science* **4**, 1583 (2022).
- ³K. Zhu, E. Trizio, J. Zhang, R. Hu, L. Jiang, T. Hou, and L. Bonati, “Enhanced sampling in the age of machine learning: Algorithms and applications,” *Chemical Reviews* **0** (0), 10.1021/acs.chemrev.5c00700, pMID: 41124671, <https://doi.org/10.1021/acs.chemrev.5c00700>.

- ⁴P. Kang, E. Trizio, and M. Parrinello, "Computing the committor with the committor to study the transition state ensemble," *Nature Computational Science*, 1–10 (2024).
- ⁵E. Trizio, P. Kang, and M. Parrinello, "Everything everywhere all at once: a probability-based enhanced sampling approach to rare events," *Nature Computational Science*, 1–10 (2025).
- ⁶M. Invernizzi and M. Parrinello, "Rethinking metadynamics: from bias potentials to probability distributions," *The Journal of Physical Chemistry Letters* **11**, 2731–2736 (2020).
- ⁷E. Trizio, A. Rizzi, P. M. Piaggi, M. Invernizzi, and L. Bonati, "Advanced simulations with plumed: Opes and machine learning collective variables," arXiv preprint arXiv:2410.18019 (2024).
- ⁸E. Weinan and E. Vanden-Eijnden, "Transition-path theory and path-finding algorithms for the study of rare events," *Annual review of physical chemistry* **61**, 391–420 (2010).
- ⁹P. G. Bolhuis, C. Dellago, and D. Chandler, "Reaction coordinates of biomolecular isomerization," *Proceedings of the National Academy of Sciences* **97**, 5877–5882 (2000).
- ¹⁰A. Ma and A. R. Dinner, "Automatic method for identifying reaction coordinates in complex systems," *The Journal of Physical Chemistry B* **109**, 6769–6779 (2005).
- ¹¹A. Berezhkovskii and A. Szabo, "One-dimensional reaction coordinates for diffusive activated rate processes in many dimensions," *The Journal of chemical physics* **122** (2005).
- ¹²B. Peters and B. L. Trout, "Obtaining reaction coordinates by likelihood maximization," *The Journal of Chemical Physics* **125**, 054108 (2006), https://pubs.aip.org/aip/jcp/article-pdf/doi/10.1063/1.2234477/15386568/054108_1_online.pdf.
- ¹³W. E. and E. Vanden-Eijnden, "Towards a Theory of Transition Paths," *Journal of Statistical Physics* **123**, 503–523 (2006).
- ¹⁴Q. Li, B. Lin, and W. Ren, "Computing committor functions for the study of rare events using deep learning," *The Journal of Chemical Physics* **151** (2019).
- ¹⁵Y. Khoo, J. Lu, and L. Ying, "Solving for high-dimensional committor functions using artificial neural networks," *Research in the Mathematical Sciences* **6**, 1–13 (2019).
- ¹⁶G. M. Rotskoff, A. R. Mitchell, and E. Vanden-Eijnden, "Active importance sampling for variational objectives dominated by rare events: Consequences for optimization and generalization," in *Proceedings of the 2nd Mathematical and Scientific Machine Learning Conference*, Proceedings of Machine Learning Research, Vol. 145, edited by J. Bruna, J. Hesthaven, and L. Zdeborova (PMLR, 2022) pp. 757–780.
- ¹⁷Z. He, C. Chipot, and B. Roux, "Committor-consistent variational string method," *The Journal of Physical Chemistry Letters* **13**, 9263–9271 (2022).
- ¹⁸Y. Chen, J. Hoskins, Y. Khoo, and M. Lindsey, "Committor functions via tensor networks," *Journal of Computational Physics* **472**, 111646 (2023).
- ¹⁹H. Chen, B. Roux, and C. Chipot, "Discovering reaction pathways, slow variables, and committor probabilities with machine learning," *Journal of Chemical Theory and Computation* (2023).
- ²⁰H. Jung, R. Covino, A. Arjun, C. Leitold, C. Dellago, P. G. Bolhuis, and G. Hummer, "Machine-guided path sampling to discover mechanisms of molecular self-organization," *Nature Computational Science*, 1–12 (2023).
- ²¹A. R. Mitchell and G. M. Rotskoff, "Committor guided estimates of molecular transition rates," *Journal of Chemical Theory and Computation* **20**, 9378–9393 (2024), pMID: 39420582, <https://doi.org/10.1021/acs.jctc.4c00997>.
- ²²S. V. Krivov, "Nonparametric analysis of nonequilibrium simulations," *Journal of Chemical Theory and Computation* **17**, 5466–5481 (2021), pMID: 34464134, <https://doi.org/10.1021/acs.jctc.1c00218>.
- ²³P. G. Bolhuis, D. Chandler, C. Dellago, and P. L. Geissler, "Transition path sampling: Throwing ropes over rough mountain passes, in the dark," *Annual Review of Physical Chemistry* **53**, 291–318 (2002).
- ²⁴P. G. Bolhuis and G. Csányi, "Nested transition path sampling," *Phys. Rev. Lett.* **120**, 250601 (2018).
- ²⁵C. Dellago, P. Bolhuis, and P. Geissler, "Transition path sampling methods," in *Computer Simulations in Condensed Matter Systems: From Materials to Chemical Biology Volume 1*, edited by M. Ferrario, G. Ciccotti, and K. Binder (Springer Berlin Heidelberg, Berlin, Heidelberg, 2006) pp. 349–391.
- ²⁶L. Onsager, "Initial recombination of ions," *Phys. Rev.* **54**, 554–557 (1938).
- ²⁷A. Kolmogoroff, "Über die analytischen methoden in der wahrscheinlichkeitsrechnung," *Mathematische Annalen* **104**, 415–458 (1931).
- ²⁸S. Das, U. Raucci, E. Trizio, P. Kang, R. P. Neves, M. J. Ramos, and M. Parrinello, "A machine learning-driven, probability-based approach to enzyme catalysis," *ACS Catalysis* **0**, 9785–9792 (0).
- ²⁹A. Berselli, E. Trizio, U. Raucci, M. J. Ramos, M. C. Menziani, F. Muniz-Miranda, and M. Parrinello, "Petase learns from lcc: reprogramming enzymatic reactivity with probability-based simulations," *ChemRxiv* **2026** (2026), 10.26434/chemrxiv.10001741/v1, <https://chemrxiv.org/doi/pdf/10.26434/chemrxiv.10001741/v1>.
- ³⁰Y. Deng, P. Kang, X. Xu, H. Li, and M. Parrinello, "The role of fluctuations in the nucleation process," *Proceedings of the National Academy of Sciences* **123**, e2526954123 (2026), <https://www.pnas.org/doi/pdf/10.1073/pnas.2526954123>.
- ³¹F. M. Dietrich, X. R. Advincula, G. Gobbo, M. A. Bellucci, and M. Salvalaglio, "Machine learning nucleation collective variables with graph neural networks," *Journal of Chemical Theory and Computation* **20**, 1600–1611 (2024), pMID: 37877821, <https://doi.org/10.1021/acs.jctc.3c00722>.
- ³²P. Kang, J. Zhang, E. Trizio, T. Hou, and M. Parrinello, "Committors without descriptors," *Journal of Chemical Theory and Computation* **0**, null (2026), pMID: 41672059, <https://doi.org/10.1021/acs.jctc.5c01848>.
- ³³A. Paszke, S. Gross, F. Massa, A. Lerer, J. Bradbury, G. Chanan, T. Killeen, Z. Lin, N. Gimelshein, L. Antiga, *et al.*, "Pytorch: An imperative style, high-performance deep learning library," *Advances in Neural Information Processing Systems* **32** (2019), 10.48550/arXiv.1912.01703.
- ³⁴L. Bonati, V. Rizzi, and M. Parrinello, "Data-driven collective variables for enhanced sampling," *The journal of physical chemistry letters* **11**, 2998–3004 (2020).
- ³⁵E. Trizio and M. Parrinello, "From enhanced sampling to reaction profiles," *The Journal of Physical Chemistry Letters* **12**, 8621–8626 (2021).
- ³⁶J. Yin, N. M. Henriksen, D. R. Slochow, M. R. Shirts, M. W. Chiu, D. L. Mobley, and M. K. Gilson, "Overview of the sampl5 host–guest challenge: Are we doing better?" *Journal of computer-aided molecular design* **31**, 1–19 (2017).
- ³⁷S. Bhakat and P. Söderhjelm, "Resolving the problem of trapped water in binding cavities: prediction of host–guest binding free energies in the sampl5 challenge by funnel metadynamics," *Journal of computer-aided molecular design* **31**, 119–132 (2017).
- ³⁸V. Rizzi, L. Bonati, N. Ansari, and M. Parrinello, "The role of water in host-guest interaction," *Nature Communications* **12**, 93 (2021).
- ³⁹D. Ray, E. Trizio, and M. Parrinello, "Deep learning collective variables from transition path ensemble," *The Journal of Chemical Physics* **158** (2023).
- ⁴⁰H. Niu, P. M. Piaggi, M. Invernizzi, and M. Parrinello, "Molecular dynamics simulations of liquid silica crystallization," *Proceedings of the National Academy of Sciences* **115**, 5348–5352 (2018), <https://www.pnas.org/doi/pdf/10.1073/pnas.1803919115>.
- ⁴¹L. Bonati, G. Piccini, and M. Parrinello, "Deep learning the slow modes for rare events sampling," *Proceedings of the National Academy of Sciences* **118**, e2113533118 (2021).
- ⁴²P. M. Piaggi and M. Parrinello, "Calculation of phase diagrams in the multithermal-multibaric ensemble," *The Journal of Chemical Physics* **150**, 244119 (2019).
- ⁴³L. Bonati, E. Trizio, A. Rizzi, and M. Parrinello, "A unified framework for machine learning collective variables for enhanced sampling simulations: mlcolvar," *The Journal of Chemical Physics* **159**, 014801 (2023), <https://pubs.aip.org/aip/jcp/article>

- pdf/doi/10.1063/5.0156343/18031428/014801_1_5.0156343.pdf.
- ⁴⁴T. P. consortium, “Promoting transparency and reproducibility in enhanced molecular simulations,” *Nature Methods* **16**, 670–673 (2019).
- ⁴⁵M. J. Abraham, T. Murtola, R. Schulz, S. Pall, J. C. Smith, B. Hess, and E. Lindahl, “Gromacs: High performance molecular simulations through multi-level parallelism from laptops to supercomputers,” *SoftwareX* **1**, 19–25 (2015).
- ⁴⁶G. A. Tribello, M. Bonomi, D. Branduardi, C. Camilloni, and G. Bussi, “PLUMED 2: New feathers for an old bird,” *Computer physics communications* **185**, 604–613 (2014).
- ⁴⁷R. Salomon-Ferrer, D. A. Case, and R. C. Walker, “An overview of the amber biomolecular simulation package,” *WIREs Computational Molecular Science* **3**, 198–210 (2013), <https://wires.onlinelibrary.wiley.com/doi/pdf/10.1002/wcms.1121>.
- ⁴⁸T. D. Kühne, M. Iannuzzi, M. Del Ben, V. V. Rybkin, P. Seewald, F. Stein, T. Laino, R. Z. Khaliullin, O. Schütt, F. Schiffmann, D. Golze, J. Wilhelm, S. Chulkov, M. H. Bani-Hashemian, V. Weber, U. Borstnik, M. TAILLEFUMIER, A. S. Jakobovits, A. Lazzaro, H. Pabst, T. Müller, R. Schade, M. Guidon, S. Andermatt, N. Holmberg, G. K. Schenter, A. Hehn, A. Bussy, F. Belleflamme, G. Tabacchi, A. Glöß, M. Lass, I. Bethune, C. J. Mundy, C. Plessl, M. Watkins, J. VandeVondele, M. Krack, and J. Hutter, “CP2K: An electronic structure and molecular dynamics software package - quickstep: Efficient and accurate electronic structure calculations,” *The Journal of Chemical Physics* **152**, 194103 (2020).
- ⁴⁹G. Bussi, D. Donadio, and M. Parrinello, “Canonical sampling through velocity rescaling,” *The Journal of Chemical Physics* **126**, 014101 (2007), https://pubs.aip.org/aip/jcp/article-pdf/doi/10.1063/1.2408420/15393604/014101_1_online.pdf.
- ⁵⁰J. Wang, R. M. Wolf, J. W. Caldwell, P. A. Kollman, and D. A. Case, “Development and testing of a general amber force field,” *Journal of computational chemistry* **25**, 1157–1174 (2004).
- ⁵¹C. I. Bayly, P. Cieplak, W. Cornell, and P. A. Kollman, “A well-behaved electrostatic potential based method using charge restraints for deriving atomic charges: the resp model,” *The Journal of Physical Chemistry* **97**, 10269–10280 (1993).
- ⁵²W. L. Jorgensen, J. Chandrasekhar, J. D. Madura, R. W. Impey, and M. L. Klein, “Comparison of simple potential functions for simulating liquid water,” *The Journal of chemical physics* **79**, 926–935 (1983).
- ⁵³V. Limongelli, M. Bonomi, and M. Parrinello, “Funnel metadynamics as accurate binding free-energy method,” *Proceedings of the National Academy of Sciences* **110**, 6358–6363 (2013).
- ⁵⁴S. Perez-Conesa, P. M. Piaggi, and M. Parrinello, “A local fingerprint for hydrophobicity and hydrophilicity: From methane to peptides,” *The Journal of chemical physics* **150** (2019).
- ⁵⁵A. P. Thompson, H. M. Aktulga, R. Berger, D. S. Bolintineanu, W. M. Brown, P. S. Crozier, P. J. in’t Veld, A. Kohlmeyer, S. G. Moore, T. D. Nguyen, *et al.*, “LAMMPS—a flexible simulation tool for particle-based materials modeling at the atomic, meso, and continuum scales,” *Comput. Phys. Commun.* **271**, 108171 (2022).
- ⁵⁶F. H. Stillinger and T. A. Weber, “Computer simulation of local order in condensed phases of silicon,” *Physical review B* **31**, 5262 (1985).
- ⁵⁷G. J. Martyna, D. J. Tobias, and M. L. Klein, “Constant pressure molecular dynamics algorithms,” *J. chem. Phys* **101**, 10–1063 (1994).

Supporting Information

S1. REFORMULATION OF KOLMOGOROV FUNCTIONAL

Here, we outline the steps leading to the simplified variational principle proposed here. For compactness, we drop the dependence on atomic coordinates and descriptors, i.e., $\mathbf{q}(\mathbf{d}(\mathbf{x})) \rightarrow \mathbf{q}$.

To compute $K[\mathbf{q}] = \langle |\nabla \mathbf{q}|^2 \rangle$, we sum over the 3 spatial dimensions l and the N atoms \mathbf{n} .

$$K[\mathbf{q}] = \langle |\nabla \mathbf{q}|^2 \rangle = \left\langle \sum_l^3 \sum_n^N \left(\frac{\partial \mathbf{q}}{\partial \mathbf{u}_{l,n}} \right)^2 \right\rangle \quad (\text{S1})$$

where \mathbf{u} denotes the mass-scaled Cartesian coordinates. We can then re-write the derivatives in the last term using the chain rule. We first take the derivatives of \mathbf{q} with respect to descriptor i , and then of descriptor i with respect to atom \mathbf{n} . The resulting expression is written as a sum over the N_d descriptors (index i), in addition to the sums over the atoms \mathbf{n} and the Cartesian components l .

$$\left\langle \sum_l^3 \sum_n^N \left(\frac{\partial \mathbf{q}}{\partial \mathbf{u}_{l,n}} \right)^2 \right\rangle = \left\langle \sum_l^3 \sum_n^N \left(\sum_i^{N_d} \frac{\partial d_i}{\partial \mathbf{u}_{l,n}} \frac{\partial \mathbf{q}}{\partial d_i} \right)^2 \right\rangle \quad (\text{S2})$$

We can now expand the object in the parentheses. To keep track of the cross elements, we need to split the descriptor indices, i.e., $i \rightarrow i, j$

$$\left\langle \sum_l^3 \sum_n^N \left(\sum_i^{N_d} \frac{\partial d_i}{\partial \mathbf{u}_{l,n}} \frac{\partial \mathbf{q}}{\partial d_i} \right)^2 \right\rangle = \left\langle \sum_l^3 \sum_n^N \sum_{i,j}^{N_d} \frac{\partial d_i}{\partial \mathbf{u}_{l,n}} \frac{\partial \mathbf{q}}{\partial d_i} \frac{\partial d_j}{\partial \mathbf{u}_{l,n}} \frac{\partial \mathbf{q}}{\partial d_j} \right\rangle \quad (\text{S3})$$

Since the derivatives of \mathbf{q} with respect to the descriptors do not depend on atom indices, the coordinate-dependent terms can be grouped separately. The sums over atoms and spatial components can thus be collected into a purely geometric factor that depends only on the descriptor gradients with respect to the atomic coordinates. The remaining factor depends exclusively on the derivatives of \mathbf{q} in descriptor space.

$$\left\langle \sum_l^3 \sum_n^N \sum_{i,j}^{N_d} \frac{\partial d_i}{\partial \mathbf{u}_{l,n}} \frac{\partial \mathbf{q}}{\partial d_i} \frac{\partial d_j}{\partial \mathbf{u}_{l,n}} \frac{\partial \mathbf{q}}{\partial d_j} \right\rangle = \left\langle \sum_{i,j}^{N_d} \left(\sum_l^3 \sum_n^N \frac{\partial d_i}{\partial \mathbf{u}_{l,n}} \frac{\partial d_j}{\partial \mathbf{u}_{l,n}} \right) \frac{\partial \mathbf{q}}{\partial d_i} \frac{\partial \mathbf{q}}{\partial d_j} \right\rangle \quad (\text{S4})$$

This way, the functional can be decoupled in two contributions: a geometric term determined by the descriptor set and a model-dependent one, constructed from the descriptor derivatives of \mathbf{q} .

$$K[\mathbf{q}] = \left\langle \sum_{i,j}^{N_d} \underbrace{\left(\sum_l^3 \sum_n^N \frac{\partial d_i}{\partial \mathbf{u}_{l,n}} \frac{\partial d_j}{\partial \mathbf{u}_{l,n}} \right)}_{g_{ij}} \underbrace{\frac{\partial \mathbf{q}}{\partial d_i} \frac{\partial \mathbf{q}}{\partial d_j}}_{k_{ij}} \right\rangle = \left\langle \sum_{i,j}^{N_d} g_{ij} k_{ij} \right\rangle \xrightarrow{\text{implicit}} \langle g_{ij} k_{ij} \rangle \quad (\text{S5})$$

In the last step, we adopt Einstein summation convention over the descriptor indices i and j . For each configuration in the ensemble, \mathbf{G} and \mathbf{K} are symmetric matrices of size $N_d \times N_d$. In this form, the functional can be written as the ensemble average of the contraction between the geometric and model-dependent terms,

$$\langle |\nabla \mathbf{q}|^2 \rangle = \langle g_{ij} k_{ij} \rangle \quad (\text{S6})$$

We then apply the *Cauchy-Schwarz inequality* to decouple the contributions and motivate our approach of skipping the positions dependence, which is now encoded only in g_{ij} . This leads to the inequality reported in the main text (see Eq. 9)

$$\langle g_{ij} k_{ij} \rangle^2 \leq \langle g_{ij} g_{ji} \rangle \langle k_{ij} k_{ji} \rangle \quad (\text{S7})$$

which motivates treating the geometric dependent term separately and focusing on the descriptor-space contribution in the practical implementation.

S2. COMPUTATION OF K AND G MATRICES

Instead of computing the quantity

$$k_{ij}k_{ji} = \text{tr}(\mathbf{K}^2) \quad (\text{S8})$$

via explicit matrix multiplication, it is computationally convenient to rewrite it using some elementary algebra.

For completeness, we also report similar manipulations for the \mathbf{G} matrix for the computation of

$$g_{ij}g_{ji} = \text{tr}(\mathbf{G}^2) \quad (\text{S9})$$

A. Trace identity for K

Matrix \mathbf{K} is defined component-wise as

$$k_{ij} = h_i h_j = \frac{\partial q}{\partial d_i} \frac{\partial q}{\partial d_j} \quad \text{with} \quad \mathbf{h} = \begin{pmatrix} \frac{\partial q}{\partial d_1} \\ \vdots \\ \frac{\partial q}{\partial d_{N_d}} \end{pmatrix} \quad (\text{S10})$$

In matrix form, this can be written as the outer product $\mathbf{K} = \mathbf{h}\mathbf{h}^\top$. Squaring the matrix gives

$$\mathbf{K}^2 = \mathbf{h}\mathbf{h}^\top \mathbf{h}\mathbf{h}^\top = (\mathbf{h}^\top \mathbf{h}) \mathbf{h}\mathbf{h}^\top \quad (\text{S11})$$

Taking the trace, we obtain

$$\text{tr}(\mathbf{K}^2) = \text{tr}\left((\mathbf{h}^\top \mathbf{h}) \mathbf{h}\mathbf{h}^\top\right) = (\mathbf{h}^\top \mathbf{h}) \text{tr}(\mathbf{h}\mathbf{h}^\top) \quad (\text{S12})$$

Since $\text{tr}(\mathbf{h}\mathbf{h}^\top) = \mathbf{h}^\top \mathbf{h}$, it follows that

$$\text{tr}(\mathbf{K}^2) = (\mathbf{h}^\top \mathbf{h})^2 = \|\mathbf{h}\|^4 \quad (\text{S13})$$

B. Trace identity for G

For a generic matrix \mathbf{G} , the Frobenius norm is defined as

$$\|\mathbf{G}\|_F^2 = \sum_i \sum_j g_{ij}^2 \quad (\text{S14})$$

On the other hand, using the definition of matrix multiplication,

$$(\mathbf{G}^\top \mathbf{G})_{ii} = \sum_j g_{ij}^\top g_{ji} = \sum_j g_{ji} g_{ji} \quad (\text{S15})$$

Taking the trace of $\mathbf{G}^\top \mathbf{G}$ gives

$$\text{tr}(\mathbf{G}^\top \mathbf{G}) = \sum_i (\mathbf{G}^\top \mathbf{G})_{ii} = \sum_i \sum_j g_{ji}^2 = \sum_i \sum_j g_{ij}^2 \quad (\text{S16})$$

Therefore, we can write

$$\text{tr}(\mathbf{G}^\top \mathbf{G}) = \|\mathbf{G}\|_F^2 \quad (\text{S17})$$

If matrix \mathbf{G} is symmetric ($\mathbf{G}^\top = \mathbf{G}$), then this simplifies to

$$\text{tr}(\mathbf{G}^2) = \|\mathbf{G}\|_F^2 \quad (\text{S18})$$

We now define the matrix \mathbf{G} as in Eq. 8

$$g_{ij} = \sum_l^3 \sum_n^N \frac{\partial d_i}{\partial \mathbf{u}_{l,n}} \frac{\partial d_j}{\partial \mathbf{u}_{l,n}} \quad (\text{S19})$$

Introducing

$$J_{i\alpha} = \frac{\partial d_i}{\partial \mathbf{u}_\alpha}, \quad \alpha = (n, l), \quad \alpha = 1, \dots, 3N \quad (\text{S20})$$

the matrix can be written as

$$g_{ij} = \sum_\alpha^{3N} J_{i\alpha} J_{j\alpha} \quad (\text{S21})$$

Equivalently, in matrix form,

$$\mathbf{G} = \mathbf{J}\mathbf{J}^\top \quad (\text{S22})$$

Using Eq.S18, since \mathbf{G} is symmetric, gives

$$\text{tr}(\mathbf{G}^2) = \|\mathbf{G}\|_F^2 = \|\mathbf{J}\mathbf{J}^\top\|_F^2 \quad (\text{S23})$$

S3. ALANINE DIPEPTIDE CONFORMATIONAL EQUILIBRIUM

A. Computational details

Simulations details The alanine dipeptide (Ace-Ala-Nme) simulations in vacuum were carried out targeting the NVT ensemble using the GROMACS-2024.5⁴⁵ MD engine patched with PLUMED-2.9.2^{44,46} and the Amber99-SB⁴⁷ force field with a 2 fs timestep. The Langevin dynamics is sampled with damping coefficient $\gamma_i = \frac{m_i}{\tau-t}$ with $\tau - t = 0.05$ ps and target temperature of 300 K.

Approximated committor model training details To model the committor function $q_\theta(\mathbf{x})$ at each iteration, we used the 45 distances between all heavy atoms as inputs of a neural network (NN) with architecture [45, 32, 32, 1] nodes/layer. For the optimization, we used the ADAM optimizer with an initial learning rate of 10^{-3} modulated by an exponential decay with multiplicative factor $\gamma = 0.99995$. The training was performed for 5000 epochs. The α hyperparameter in the loss function was set to 10^3 , and we optimized the log of the total loss for numerical stability. The number of iterations, the corresponding dataset size, and the λ and the OPES BARRIER used in the biased simulations with the corresponding model are summarized in Table S1 alongside the simulation time t_s and the output sampling time t_o .

TABLE S1. **Summary alanine.** Summary of the iterative procedure for alanine.

Iteration	Dataset size	OPES BARRIER [kJ/mol]	λ	t_s [ns]	t_o [ps]
0	5000	30	2	2*10	1
1	22000	30	2	2*10	1
2	40000	30	3	2*10	1

B. Additional figures

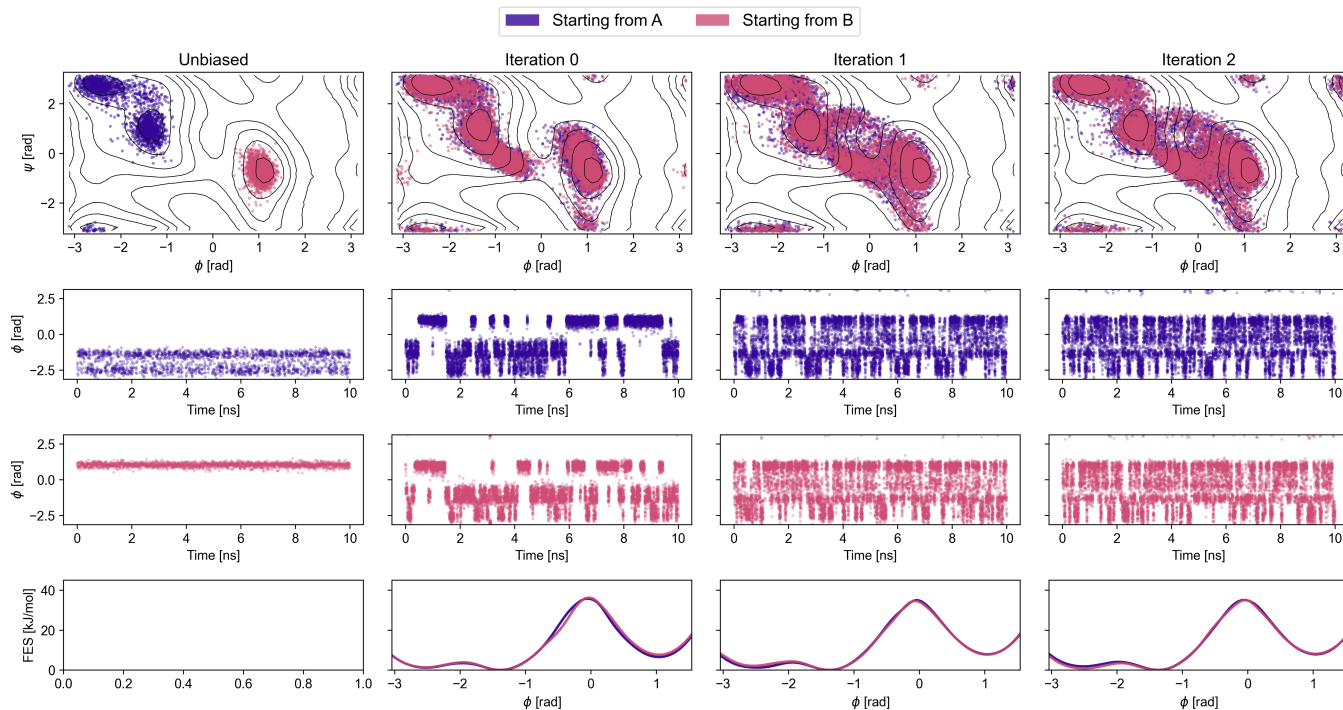


FIG. S1. **Iterative sampling on alanine.** Top row: Scatter plot of the sampled points in the $\phi\psi$ space at successive iterations. Points from trajectories initialized in state A are shown in purple, while those initialized in state B are shown in pink. Second row: Time series of the ϕ dihedral angle for trajectories started from state A. Third row: Time series of the ϕ dihedral angle for trajectories started from state B. Bottom row: Free energy surface (FES) plotted along ϕ , estimated from the sampled configurations at each iteration.

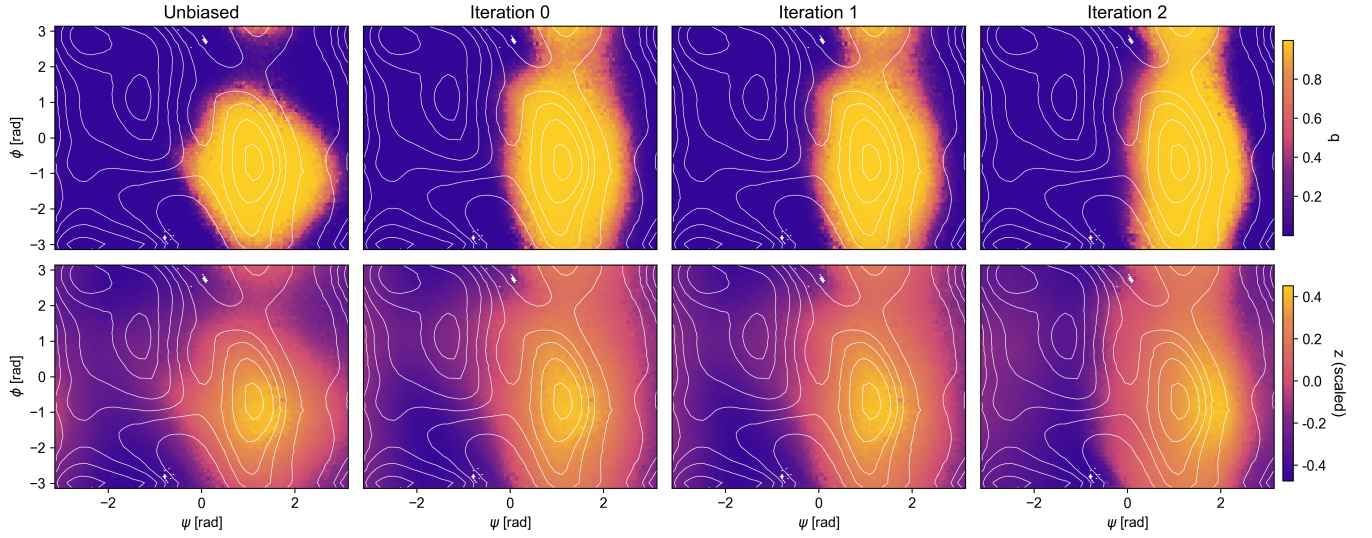


FIG. S2. **Alanine committor models.** Contour plots in the $\phi\psi$ space of the learned q (top row) model and the corresponding z (bottom row) at successive iterations. Values of the z variable are scaled to be in the $[-0.5, 0.5]$ range.

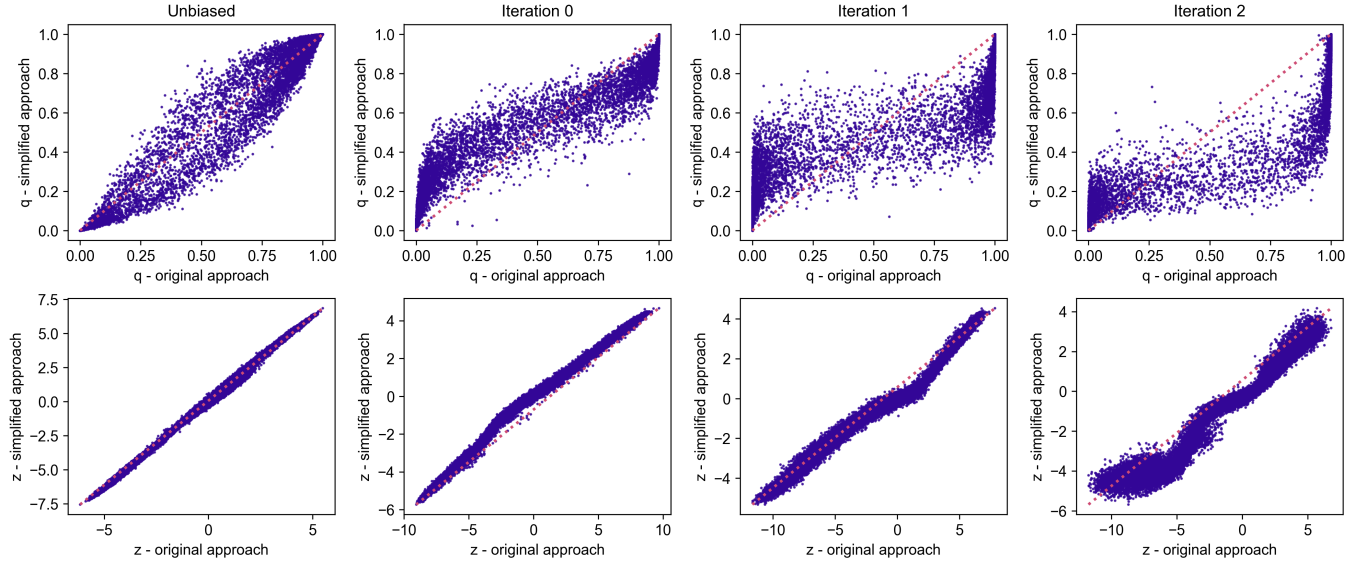


FIG. S3. **Convergence of alanine committor models.** Comparison between the q (top row) and the corresponding z learned using the original and the simplified approaches at successive iterations.

S4. TROPOLONE PROTON TRANSFER

A. Computational details

Simulations details The intramolecular proton transfer simulations were carried out targeting the NVT ensemble using the CP2K-8.1⁴⁸ software package patched with PLUMED-2.9.1⁴⁴ at PM6 semi-empirical level. The integration step was 0.5 fs and we used the velocity rescaling thermostat⁴⁹ set at 300 K with a time constant of 100 fs.

Approximated committor model training details To model the committor function $q_{\theta}(\mathbf{x})$ at each iteration, we used the 36 distances between all heavy atoms of the molecule and the distances between the reactive hydrogen and the two oxygens as inputs of a neural network (NN) with architecture [38, 16, 16, 1] nodes/layer. For the optimization, we used the ADAM optimizer with an initial learning rate of 10^{-3} modulated by an exponential decay with multiplicative factor $\gamma = 0.99995$. The training was performed for 5000 epochs in the first cycle and then 20000 epochs in the following ones. The α hyperparameter in the loss function was set to 10^3 , and we optimized the log of the total loss for numerical stability. The number of iterations, the corresponding dataset size, and the λ and the OPES BARRIER used in the biased simulations with the corresponding model are summarized in Table S2 alongside the simulation time t_s and the output sampling time t_o .

TABLE S2. **Summary tropolone PT.** Summary of the iterative procedure for intramolecular proton transfer in tropolone.

Iteration	Dataset size	OPES BARRIER [kJ/mol]	λ	t_s [ps]	t_o [ps]
0	4000	60	1.2	2*500	0.05
1	22000	60	4	2*500	0.05
2	40000	60	4	2*500	0.05

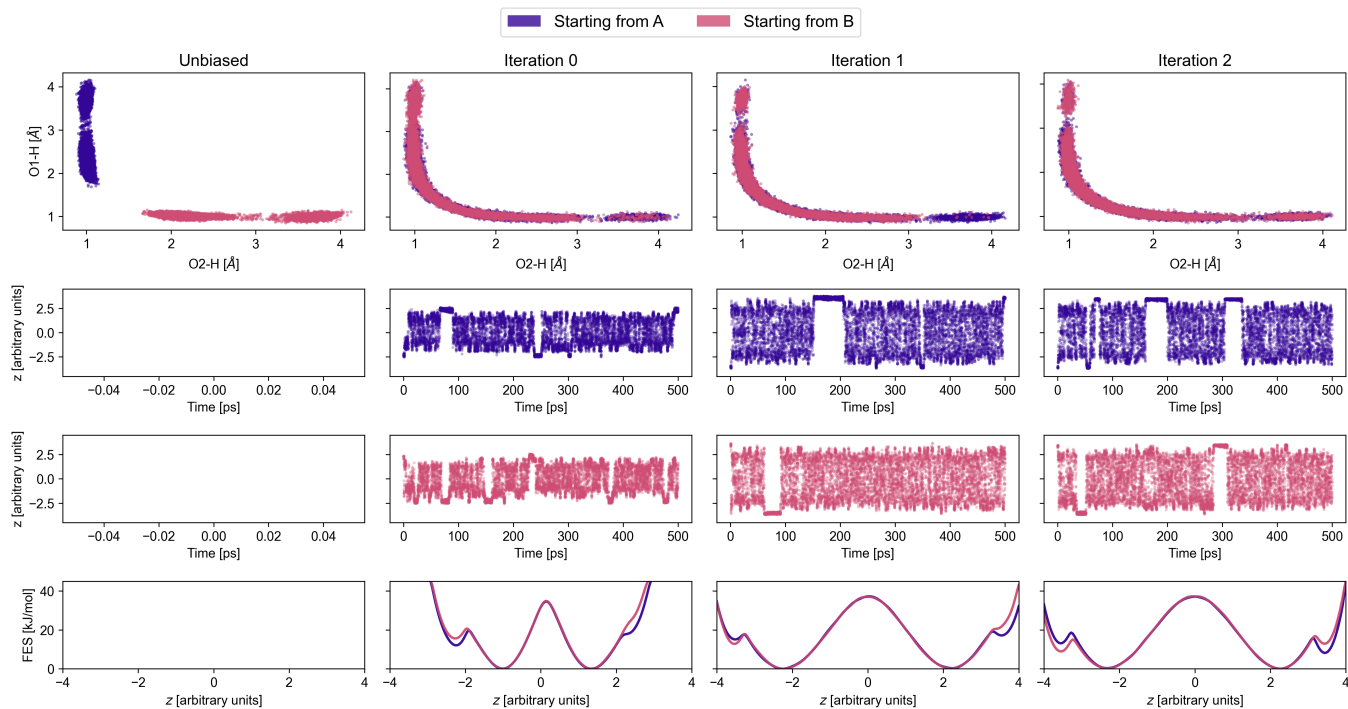


FIG. S4. **Iterative sampling on tropolone.** Top row: Scatter plot of the sampled points in the space defined by the O2-H and O1-H distances at successive iterations. Points from trajectories initialized in state A are shown in purple, while those initialized in state B are shown in pink. Second row: Time series of the z CV for trajectories started from state A. Third row: Time series of the z CV for trajectories started from state B. Bottom row: Free energy surface (FES) plotted along the z CV, estimated from the sampled configurations at each iteration.

S5. OAME-G2 BINDING

A. Computational details

Simulations details We performed the simulations with GROMACS-2024.5⁴⁵ in combination with the PLUMED-2.9.4⁴⁴ plugin. We use the GAFF⁵⁰ force field with RESP⁵¹ charges and the TIP3P⁵² water model. We set the timestep to 2 fs, targeting the NVT ensemble at 300 K via a velocity rescale thermostat⁴⁹ with a time constant of 0.1 ps. The simulation box is cubic with a side of 40.27 Å and it contains 2100 water molecules in solution together with the host OAME and the G2 guest molecule. Sodium ions are included to counterbalance excess charges. At every simulation step, the coordinates are aligned so that the vertical axis of the box coincides with the binding axis h , and the simulation box is centered on the virtual atom V1.

The funnel restraint In our simulations, we used a funnel restraint⁵³ equivalent to the one previously employed by Refs. 37,38,54 on the same system. Here, we summarize the details of such a restraint, while more details can be found in the original works. The funnel limits the space available to the ligand in the unbound state U by confining it to a cylindrical volume above the binding site. As the ligand approaches the binding site, the funnel restraint becomes wider so that its presence does not affect the binding process itself. Having aligned with PLUMED the system to a reference configuration where the binding axis is found along the vertical axis, we define h as the projection on the binding axis of the center of the carbon atoms of each ligand and r as its radial component. When $h > 10\text{Å}$, the funnel surface is a cylinder with radius $R_{\text{cyl}} = 2\text{Å}$ with its axis along the vertical direction. When $h < 10\text{Å}$, the funnel opens into an umbrella-like shape with a 45 degree angle whose surface is defined by $r = 12 - h$. The force that, for a displacement x , pushes the ligand away from the funnel’s surface is harmonic $-k_F x$ with $k_F = 20\text{ kJ/mol Å}^{-2}$. A further harmonic restraint is applied on h to prevent the ligand from getting too far from the host, reaching the upper boundary of the simulation box. The corresponding force is $-k_U(h - 18)$ for $h > 18\text{Å}$ and $k_U = 40\text{ kJ/mol Å}^{-2}$.

During training, we set boundaries further to state U so that the labeled configurations used to impose the boundary conditions will not influence the committor training in the subsequent iterative simulations. We apply the funnel restraint described above and two additional harmonic restraints $-k_U(h - 20)$ for $h > 20\text{Å}$ and $-k_U(h - 18)$ for $h < 18\text{Å}$, with $k_U = 20\text{ kJ/mol}$.

Because of the funnel presence, the free energy difference between the bound and the true unbound state that we extract from enhanced sampling simulations needs a correction that can be calculated as:

$$\Delta G = -\frac{1}{\beta} \log \left(C_0 \pi R_{\text{cyl}}^2 \int_B dh \exp[-\beta (W(h) - W_U)] \right) \quad (\text{S24})$$

where $\beta = 1/(k_B T)$, $C_0 = 1/1660\text{ Å}^{-3}$ is the standard concentration, h is the coordinate along the funnel’s axis, $W(h)$ is the free energy along the funnel axis and W_U its reference value in state U. More precisely, we define W_U as the average free energy value in the interval $1.6\text{ Å} < h < 1.8\text{ Å}$. The integral is computed over the state B region that we define as $0.3\text{ Å} < h < 0.8\text{ Å}$.

Approximated committor model training details To model the committor function $q_\theta(\mathbf{x})$ at each iteration, we used the same water coordination numbers used in Ref. 38, 8 with respect to 2.5 Å-spaced virtual atoms (V) along the binding axis and 4 with respect to 4 atoms on the ligand molecule (M) (2 on the ring (1 and 2), 2 on the terminal atoms (3 and 4)) as inputs of a neural network (NN) with architecture [12, 24, 8, 1] nodes/layer. For the optimization, we used the ADAM optimizer with an initial learning rate of 10^{-3} modulated by an exponential decay with multiplicative factor $\gamma = 0.99995$. The training was performed for 5000 epochs. The α hyperparameter in the loss function was progressively diminished through the iterations, i.e., 10^3 , 10^1 , 10^{-3} , and we optimized the log of the total loss for numerical stability. The number of iterations, the corresponding dataset size, and the λ and the OPES BARRIER used in the biased simulations with the corresponding model are summarized in Table S3 alongside the simulation time t_s and the output sampling time t_o .

TABLE S3. **Summary calixarene.** Summary of the iterative procedure for calixarene.

Iteration	Dataset size	OPES BARRIER [kJ/mol]	λ	t_s [ns]	t_o [ps]
0	4000	50	3.6	2*100	1
1	42000	50	3.6	2*100	1
2	74000	50	3.6	2*250	1

B. Additional figures

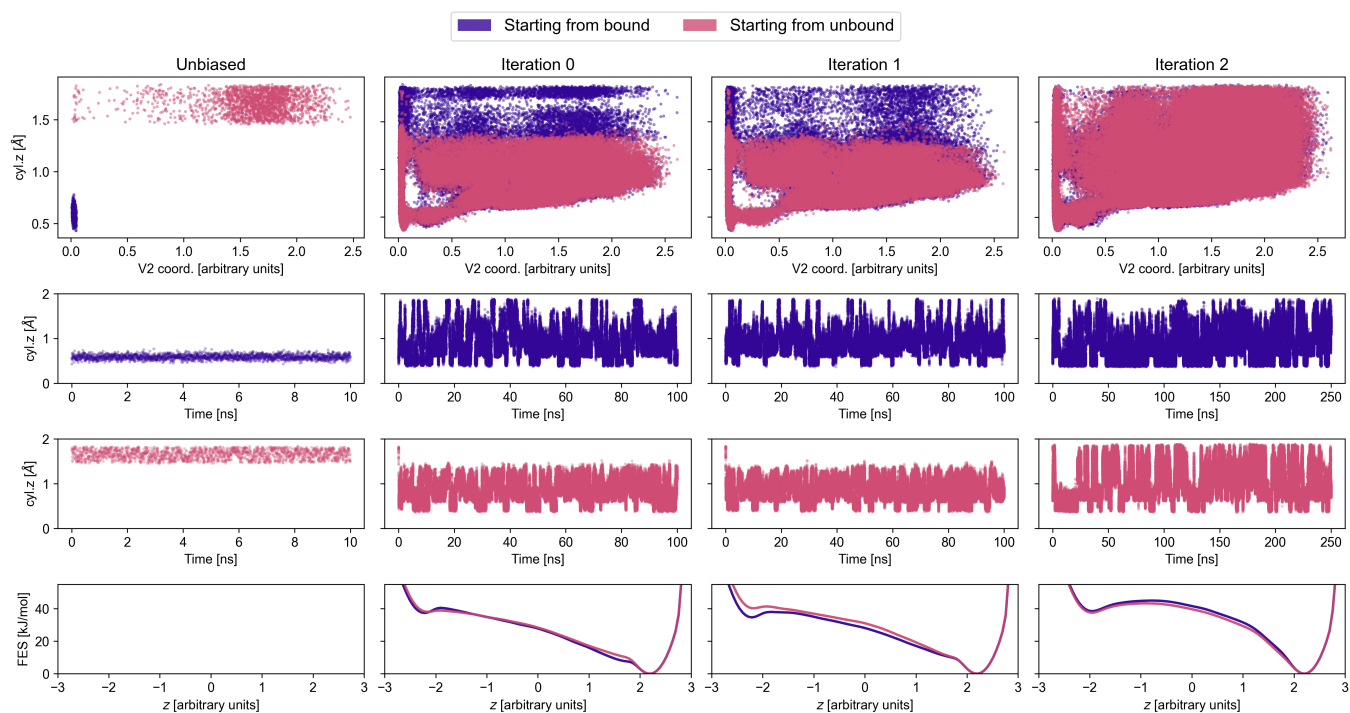


FIG. S5. **Iterative sampling on calixarene.** Top row: Scatter plot of the sampled points in the space defined by the distance from the binding pocket and the hydration of the binding pocket, at successive iterations. Points from trajectories initialized in the bound state are shown in purple, while those initialized in the unbound state are shown in pink. Second row: Time series of the distance from the binding pocket for trajectories started from state A. Third row: Time series of the distance from the binding pocket for trajectories started from state B. Bottom row: Free energy surface (FES) plotted along the z CV, estimated from the sampled configurations at each iteration.

S6. SILICON CRYSTALLIZATION

A. Computational details

Simulations details Silicon crystallization simulations were carried out targeting the NPT ensemble using the same setup of Ref.⁴¹, employing LAMMPS⁵⁵ (22Jul2025 update1) patched with PLUMED-2.9.0.⁴⁴ As an interatomic potential we used the Stillinger–Weber interatomic potential.⁵⁶ A $3 \times 3 \times 3$ supercell (216 atoms) was simulated in the isothermal–isobaric (NPT) ensemble with a time step of 2 fs. The velocity-rescaling thermostat⁴⁹ with a target temperature of 1700 K and a relaxation time of 100 fs was used, while the barostat⁵⁷ target pressure was set to 1 atm and the relaxation time to 1 ps. First, two 2 ns-long simulations of standard MD in the solid and liquid states were performed. During the simulation, we monitored the fraction of diamond-like atoms computed in PLUMED⁴⁴ with the Environment Similarity CV,⁴² with parameters $\text{SIGMA} = 0.4$, $\text{LATTICE_CONSTANTS} = 5.43$, $\text{MORE_THAN} = \{ \text{R}_0 = 0.5 \text{ NN} = 12 \text{ MM} = 24 \}$.

Approximated committor model training details To model the approximated committor, we used the 95 three-dimensional structure factor peaks as inputs of a neural network (NN) with architecture [95, 48, 24, 1] nodes/layer and an initial normalization layer. OPES+ V_K simulations biasing the committor-based z variable, with $\text{PACE} = 500$, adaptive sigma with $\text{ADAPTIVE_SIGMA_STRIDE}=500$ were performed. For the committor training, we discarded the first part of the simulations in which the bias was stabilizing. For the optimization, we used the ADAM optimizer with an initial learning rate of 10^{-3} modulated by an exponential decay with multiplicative factor $\gamma = 0.99995$. The training was performed for 5000 epochs during the first iteration and for 40000 epochs during the following ones. The α hyperparameter in the loss function was progressively diminished through the iterations, i.e., 10^3 , 10^{-3} , 10^{-6} , and we optimized the log of the total loss for numerical stability. The number of iterations, the corresponding dataset size, and the λ and the OPES BARRIER used in the biased simulations are summarized in Table S4 alongside the simulation time t_s and the output sampling time t_o . In this case, only data from the previous iteration were used for the training.

TABLE S4. **Summary silicon.** Summary of the iterative procedure for silicon crystallization.

Iteration	Dataset size	OPES BARRIER [kJ/mol]	λ	t_s [ns]	t_o [ps]
0	10000	1100	100	2*50	1
1	110000	1100	1000	2*100	1
2	110000	1100	1000	2*100	1

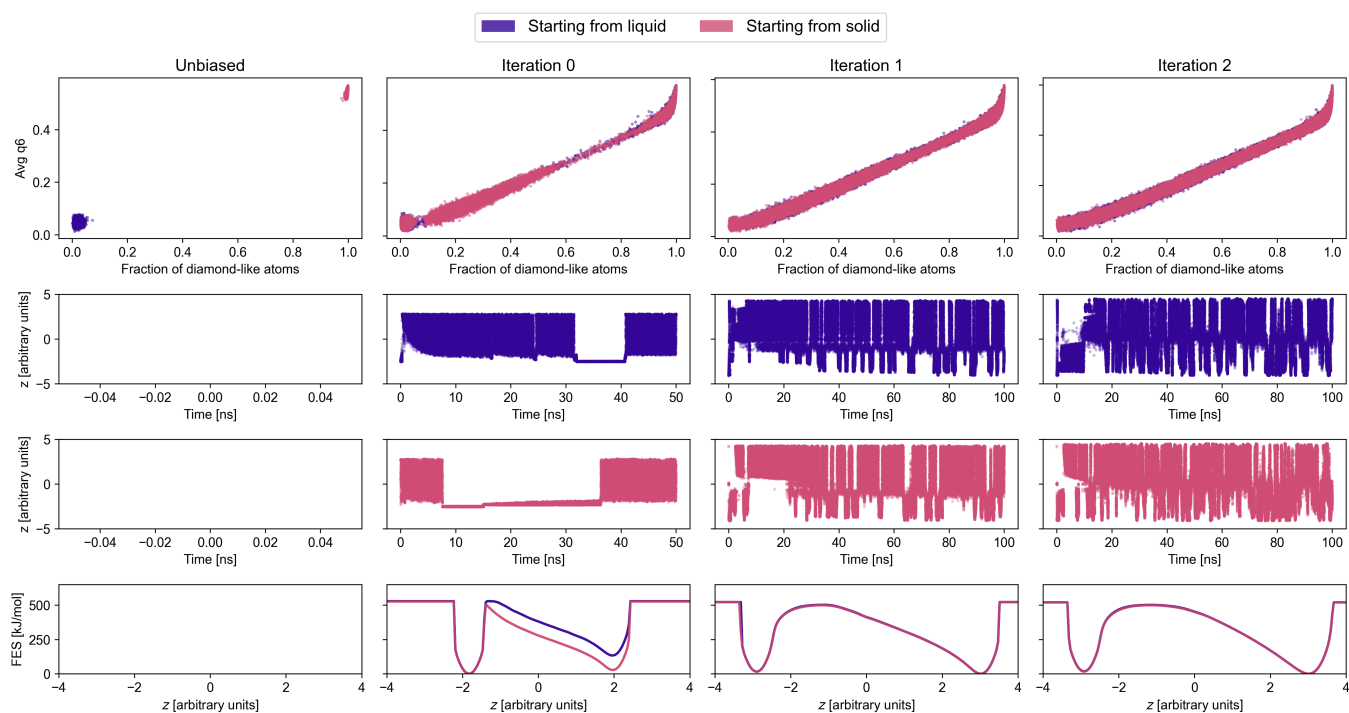


FIG. S6. **Iterative sampling on silicon.** Top row: Scatter plot of the sampled points in the space defined by the average sixth-order Steinhardt parameter q_6 and the fraction of diamond-like atoms at successive iterations. Points from trajectories initialized in state A are shown in purple, while those initialized in state B are shown in pink. Second row: Time series of the z CV for trajectories started from liquid. Third row: Time series of the z CV for trajectories started from solid. Bottom row: Free energy surface (FES) plotted along the z CV, estimated from the sampled configurations at each iteration.

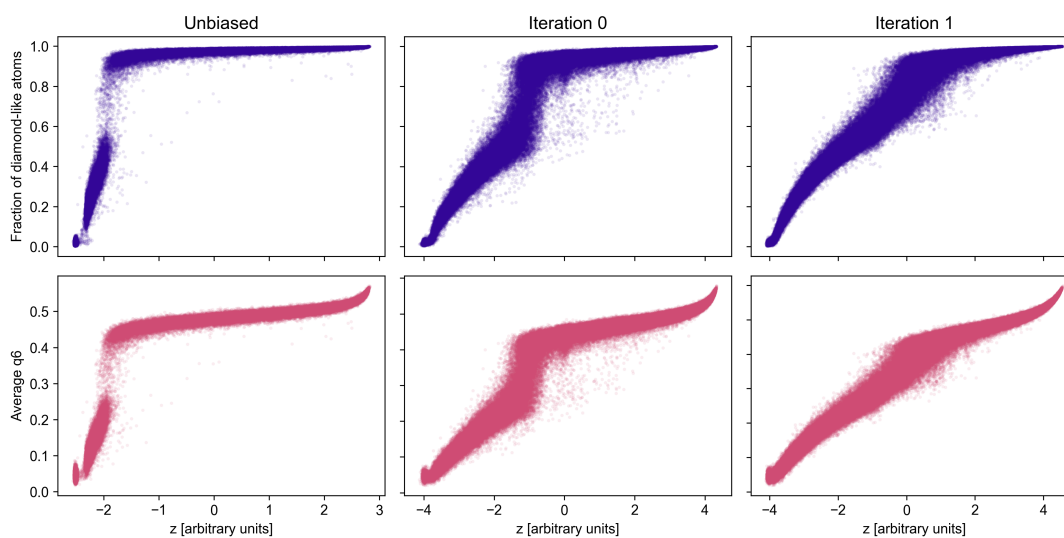


FIG. S7. **Learned models vs reference CVs.** Comparison between the learned z variable at successive iterations and reference CVs, i.e., the fraction of diamond-like atoms (top row) and the average sixth-order Steinhardt parameter (bottom row).